Capture and immobilization of gaseous ruthenium tetroxide RuO$_4$ in UiO-66-NH$_2$ Metal-Organic Framework.

Maëva LELOIRE,[1,2] Philippe NERISSON,[2] Frédérique POURPOINT,[1] Marielle HUVE,[1] Jean-François PAUL,[1] Laurent CANTREL,[2] Thierry LOISEAU,[1] Christophe VOLKRINGER[1,3*]

[1]Univ. Lille, CNRS, Centrale Lille, Univ. Artois, UMR 8181 - UCCS - Unité de Catalyse et Chimie du Solide, F-59000 Lille, France.

[2]Institut de Radioprotection et de Sureté Nucléaire (IRSN), PSN-RES/SEREX, Saint-Paul Lez Durance, 13115, France.

[3]Institut Universitaire de France, 1 rue Descartes, 75231 Paris Cedex 05, France.

KEYWORDS. RuO_4 capture, Metal-Organic Frameworks, radionuclides mitigation.

SYNOPSIS. UiO-66-NH_2 is a very efficient porous materials for the capture and the immobilization of gaseous RuO_4, a highly toxic molecule produced during a nuclear accident.

ABSTRACT.

^{106}Ru is a radioactive isotope usually generated by the nuclear industry within power plant reactor. During a nuclear accident, ^{106}Ru reacts with oxygen, leading to the production of highly volatile ruthenium tetroxide RuO_4. The combination of volatility and radioactivity makes $^{106}RuO_4$, one of the most radiotoxic species and justify the development of specific setup for its capture and immobilization. In this study, we report for the first time the capture and the immobilization of gaseous RuO_4 within a porous Metal-Organic Framework (UiO-66-NH_2). We used a specific installation for the production of gaseous RuO_4 as well as the quantification of this gas trapped within the filtering medium. We have proved that UiO-66-NH_2 has a remarkable affinity for RuO_4 capture, since this MOF exhibits the worldwide highest RuO_4 decontamination factor (DF up to 5745), hundreds of times higher than the DF values of sorbents daily used by the nuclear industry (zeolites or activated charcoal). The efficiency of UiO-66-NH_2 is explained by its pores diameter well adapted to the capture and the immobilization of RuO_4, as well as its conversion into stable RuO_2 within the pores. This conversion corresponds to the reactivity of RuO_4 with the MOF organic sub-network, leading to the oxidation of terephthalate ligands. As proved by powder X-ray diffraction or NMR, these modifications do not decompose the MOF structure.

INTRODUCTION.

Ruthenium is an important fission product generated in a power plant nuclear reactor containing uranium oxide or mixed plutonium-uranium oxides as fuel.[1] Whereas this element remains as stable metallic aggregate within the nuclear fuel (>100 kg for a 900 MWe reactor), an exposition to oxidizing atmosphere gives rise to the production of multiple stoichiometries of ruthenium oxides (RuO_n), which are susceptible to be much more volatile than its metallic form.[2] Among them, ruthenium tetroxide RuO_4 has paid a special attention for the radioprotection context. Indeed, in addition to the chemical toxicity of ruthenium, the species RuO_4 is the only ruthenium oxide occurring at the gaseous state under standard conditions,[2] and is able to disseminate radiotoxic isotopes, mainly ^{103}Ru ($T_{1/2} = 369$ days) and ^{106}Ru ($T_{1/2} = 39.3$ days).

Among the nuclear accidents that have occurred in the last 40 years, the events of Chernobyl (Ukraine) in 1986 (>200 TBq of Ru) and the undeclared major nuclear release in 2017 from Mayak (Russia) (from 100 to 300 TBq) have produced the highest amounts of radioactive Ru, that were disseminated in the atmosphere and contaminating numerous countries. Recent studies confirmed that volatile and highly reactive RuO_4 was the origin of the release of the radioactive pollution.[2-4]

While specific porous adsorbent media, like activated charcoals or silver exchanged zeolites, have been used for decades for the capture of radiotoxic gaseous iodine ($^{129/131}I$),[5] the development of specific process remains much less explored for the immobilization or the separation of gaseous RuO_4. Typically, in the spent fuel reprocessing, gaseous RuO_4 precipitates on cold surfaces as a black nonvolatile RuO_2 deposit, which makes difficult the separation from the other radioactive wastes.[6] In the case of a nuclear accident, RuO_4 can be trapped in by pool scrubbing in alkaline solution and solubilized into ruthenates (RuO_4^{2-}) and perruthenates (RuO_4^-).[7] Moreover, sand beds

and metallic filters usually mounted on Filtered Containment Venting System (FCVS) equipping nuclear power plants,[8] are not efficient enough for the RuO_4 trapping for operating conditions up to 100°C.[7] However, above 120°C, this filtration setup shows a different behavior, involving the precipitation of gaseous RuO_4 into solid RuO_2 at the surface of the sand bed and the metallic filters. The same temperature dependence and behavior were also observed with zeolites.[9-11]

In the recent research for innovative trapping compounds, Metal-Organic Frameworks (MOFs) are a class of hybrid crystalline porous solids synthesized from a variety of organic ligands and metallic cations (Zn^{2+}, Al^{3+}, Zr^{4+}, etc).[12] Thanks to their very high porosity and specific surfaces (up to 7000 m^2/g), these materials found many applications in several fields like gas sorption, catalysis or drug release.[13] So far, one notices already one industrial utilization of MOFs for the storage and safe delivery of hazardous dopant gases (arsine, phosphine, boron trifluoride), operated in electronics manufacturing.[14]

In the nuclear domain, MOF compounds have shown their efficiency for the capture and the immobilization of various radionuclides, either as solubilized cations (^{79}Se, ^{90}Sr, ^{99}Tc, ^{137}Cs, ^{232}Th, ^{238}U)[15, 16] or as gaseous species (^{131}I, ^{222}Rn).[17, 18] For these latter, MOF solids usually exhibit comparable or even better sorption properties than materials typically used in the nuclear industry, such as silver doped zeolites or activated charcoals for molecular iodine, for instance. Among the different radioactive species, pertechnetate anion TcO_4^- exhibits a tetrahedral coordination environment very similar to RuO_4. Several cationic MOFs have already shown excellent decontamination factor for this species, even in the presence of competitive anions.[19-21]

These good porosity performances are not altered under the accidental context, since some MOFs show great resistance under drastic conditions encountered during a nuclear accident, involving

radiations,[22] relative high temperature and steam.[23] This is the case of the zirconium aminoterephtalate MOF called UiO-66-NH$_2$, which is stable in severe nuclear accidental conditions and without the release of trapped radioactive iodine ^{131}I.[18] This good affinity for molecular iodine was assigned to the presence of amino groups attached to the hybrid framework and enhancing stable charge transfer complex with iodine.[24]

Whereas DFT calculations indicate that porous MOF compounds could be good candidates for the trapping of gaseous RuO$_4$,[25] no investigation has been experimentally carried out to evaluate their efficiency (as well as other porous materials) for the filtration of this particular gas. This lack of knowledge can be attributed to the difficulty to generate a stable flow without the decomposition of RuO$_4$, as well as to quantify and characterize ruthenium species trapped within the porous matrix.

In this study, we report for the first time the capture and the immobilization of gaseous RuO$_4$ within a porous Metal-Organic Framework. Our choice orientated to the Zr-based MOF UiO-66-NH$_2$,[26] due to its great stability under severe conditions as mentioned above,[23] a very good affinity for iodine, its straightforward synthesis, but also its structural organization, that we suppose well adapted for the capture and the confinement of RuO$_4$. Indeed, UiO-66-NH$_2$ (Figure 1) is built from the assembly of Zr-centered oxo/hydroxo hexanuclear clusters with aminoterephtalate ligands, giving rise to two types of cavities (octahedral or tetrahedral shape), which are accessible through windows slightly larger (5 Å) than the estimated diameter of RuO$_4$ (4.5 Å). As already proved with gaseous iodine (~3.3 Å) trapped within ZIF-8 (pore aperture of 3.4 Å),[27, 28] this structural feature should allow the diffusion of the gaseous species (in our case RuO$_4$) within the pores while limiting its releasing.

Furthermore, the presence of amino functional group within the pore could improve the immobilization of RuO_4 within the pores through hydrogen bonding.[25]
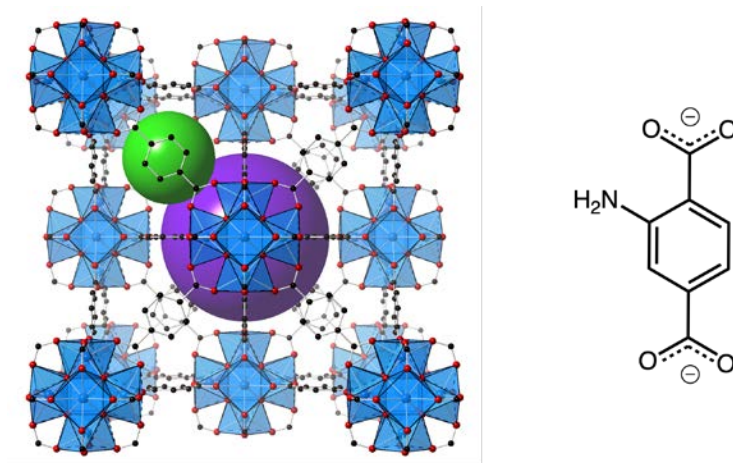
Figure 1. Structure of UiO-66-NH$_2$ and representation of aminoterephtalate ligand. Green and purple spheres correspond to tetrahedral and octahedral cavities, respectively.

For this work, we used an experimental setup devoted to RuO_4 dynamic filtration test at 50°C. After the filtration step, the loaded UiO-66-NH$_2$ sample will be deeply characterized by means of numerous techniques of characterization (X-ray diffraction, solid state NMR, electronic microscopy, gas sorption, etc.), in order to determine the quantity and the behavior of ruthenium within the pores.

MATERIALS AND METHODS.

Materials and Chemicals.

Zirconium chloride ($ZrCl_4$, 99.5%, from Alfa Aesar), 2-aminoterephtalic acid ($H_2BDC-NH_2$, 99.0%, from Alfa Aesar), formic acid (HCOOH, 99.9%, from Acros Organics),

dimethylformamide (DMF, 98%, from Fisher Scientific), methanol (98%, VWR), $RuO_2 \cdot xH_2O$ (Acros Organics 54%w Ru).

Synthesis and characterization of UiO-66-NH2.

UiO-66-NH$_2$ was synthesized in a 1L Schott DURAN$^{®}$ pressure bottle under. 4 g of $ZrCl_4$ (17.16 mmol) and 6 g of H$_2$BDC-NH$_2$ were added to a mixture of DMF (650 ml) and formic acid (32 ml). The solution was heated under static conditions at 120°C during 24h, then cooled to room temperature. The resulting solid was collected by centrifugation and redispersed in 1L of fresh DMF during 24h (3 times) and then in fresh methanol during 24h (3 times). After a centrifugation step, the solid was dried at 100°C during 1 h and then at 150°C during 8 h. Before RuO$_4$ filtration, the solid was placed in a closed vial and stored in a O$_2$/H$_2$O free glove box (Ar).

Pristine and RuO$_4$ impregnated UiO-66-NH$_2$ were thoroughly characterized by means of several techniques. The crystallinity of the solids was characterized at room temperature by powder x-ray diffraction (PXRD, D8 advance A25 Bruker apparatus equipped with Bragg-Brentano geometry), ranging from 3 to 50° (2θ), a step length of 0.02° (2θ) and a counting time of 0.5 sec/step.

The specific surface area was determined by nitrogen adsorption at 77 K using a Micromeritics ASAP 2020 apparatus. Specific surface area was calculated in the p/p_0 range: 0.015-0.3 using the Brunauer-Emmett-Teller (BET) method. Before the sorption measurements, the samples were outgassed at 150°C under secondary vacuum during 15 h.

IR spectra were measured on a Perkin-Elmer Spectrum Two spectrometer, equipped with a diamond attenuated total reflectance (ATR) accessory between 4000 and 400 cm^{-1}.

The thermal stability of pristine and RuO_4 loaded UiO-66-NH_2 was analyzed by themogravimetric analysis (TGA 92 Setaram, under air, 5°C/min) and thermodiffraction. X-ray thermodiffractometry was performed under 5 L.h^{-1} air flow in an Anton Parr HTK1200N of a D8 Advance Bruker Diffractometer (CuKα) equipped with a Vantec 1 linear position sensitive detector. Each powder pattern was recorded in the range 5-60° (2θ) (at intervals of 20 to 800 °C), with a 0.5 s/step scan, corresponding to a duration of approximatively 30 min. The temperature ramps between two patterns were 0.08°C^{-1} to 800°C.

TEM measurements were conducted on the TEM FEI TITAN Themis 300 (300 kV). It is equipped with a probe corrector for resolution of 0.7 Å in STEM mode, a Super-X quad EDS detector for elemental analysis. The powder was crushed and dropped in the form of alcohol suspension on carbon supported copper grids, followed by evaporation under ambient condition.

Solid state NMR experiments were carried out on a Bruker Advance III 9.4 T spectrometer (400 MHz and 100.6 MHz for ^{1}H and ^{13}C respectively) equipped with a 4 mm double resonance probe spinning at a frequency of ν_R=12.5 kHz. ^{13}C spectra was recorded using a cross polarization experiment (CPMAS). The first $\pi/2$ ^{1}H rf-field (radio-frequency) amplitude was 58 kHz. During the contact, a ^{13}C rf-field amplitude of 70 kHz and a linear ramp from 29 to 58 kHz on the ^{1}H channel were used. The contact time was t_{cp} = 1500 ms. A recycling delay of 1 s and a number of scans of 2048 and 51200 for the UiO-66-NH_2 and the RuO_4 loaded UiO-66-NH_2 were used, respectively. A SPINAL-64 decoupling sequence of 58 kHz was used during the acquisition.[29] The ^{13}C chemical shifts were referenced using the CH group of adamantane at 29.47 ppm.

Experimental setup for the production and the filtration of gaseous RuO₄.
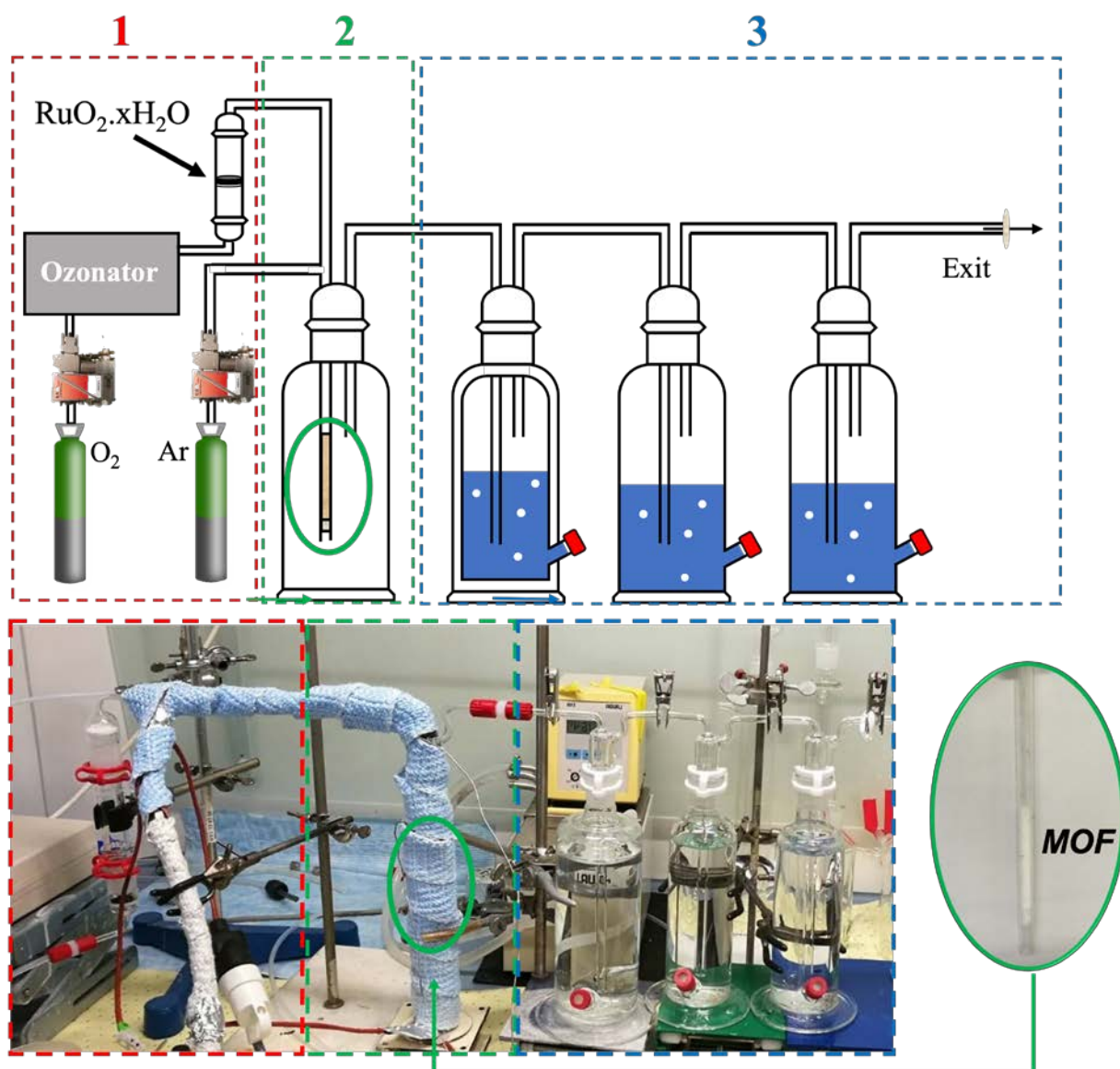
Figure 2. Scheme (top) and photography (bottom) of the experimental setup dedicated to the production and the quantification of $RuO_4(g)$ trapped within UiO-66-NH$_2$. For clarity, the different parts are surrounded

by a colored line, red for $RuO_{4(g)}$ generation (1), green for filtration in UiO-66-NH$_2$ (2) and blue for quantification (3).

The experimental bench used in this study (Figure 2) is partitioned into three modules, corresponding respectively to the generation (1), the filtration (2) and the trapping of RuO$_4$ for quantification (3).
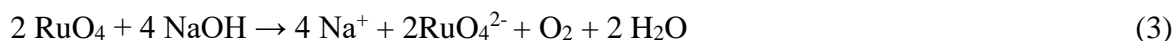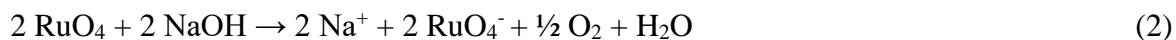
The generation of gaseous $RuO_{4(g)}$ (1) is carried out in a glass column (height: 10 cm; diameter: 2 cm), containing commercial black powder of $RuO_2 \cdot xH_2O$ ($\approx$ 550 mg, Merck manufacturer data 54% wt of Ru), and delimited by two sintered glass filters at each end of the column. $RuO_{4(g)}$ is obtained by the ozonation RuO$_2$ according to equation 1.

$$RuO_2 \text{ (s)} + 2/3 \text{ } O_3 \text{ (g)} \rightarrow RuO_4 \text{ (g)} \tag{1}$$

Ozone is produced by a specific generator (Anseros brand ozonator) from oxygen. With an O$_2$ flow rate equal to 0.06 nL.min^{-1}, the ozone concentration is stabilized at [O$_3$] = 75 g.m^{-3}, at room temperature.

The resulting orange gaseous stream contains a mixture of $RuO_{4(g)}$, oxygen and ozone, is directed to the filtration device heated at 50°C. In this module corresponding to a glass rod (length: 10 cm, diameter: 0.5 cm), powdered UiO-66-NH$_2$ is placed on a piece of rock wool as an inert support. 95 mg of dried UiO-66-NH$_2$ were used for this study. Upstream the filtration step, the addition of an inert carrier gas (Ar) allows to adjust and stabilize the stream velocity around 10 cm.s^{-1}, which corresponds to the expected maximum velocity in a filtration device, in nuclear reactor accidental situation.

After the filtration step, the resulting flow is directed to the three successive bubblers (Figure 3) containing sodium hydroxide aqueous solution (NaOH, 0.05 M), for the trapping of $RuO_{4(g)}$ not having be adsorbed by UiO-66-NH$_2$. In the basic solution, RuO_4 is dissolved into perruthenate (RuO_4^-) and ruthenate (RuO_4^{2-}) species according to the equations (2) and (3):

$$2\ RuO_4 + 2\ NaOH \rightarrow 2\ Na^+ + 2\ RuO_4^- + \tfrac{1}{2}\ O_2 + H_2O \tag{2}$$

$$2\ RuO_4 + 4\ NaOH \rightarrow 4\ Na^+ + 2RuO_4^{2-} + O_2 + 2\ H_2O \tag{3}$$

The first bubbler is equipped with a double jacket allowing it to be cooled by water at 5°C for an efficient trapping of $RuO_{4(g)}$.[30] The following bubblers are at room temperature and without double jacket and ensure a full and safe trap of any residual $RuO_{4(g)}$ by bubbling, before discharge to the fume hood. The solubilization of $RuO_{4(g)}$ and its chemical trapping is confirmed by the color change of the solution, from colorless to brown-yellow (Figure 3a).

Samples (5 mL) of solution from each bubbler are taken during the experiment and then analyzed by ICP-AES (Perkins) to determine decontamination factor and the quantity of ruthenium trapped by the UiO-66-NH$_2$ compound. By this method, we confirmed the linear production of $RuO_{4(g)}$ (Figure 3b) during the experimental time used for the filtration test (135 min) and the calculated average production of RuO_4 generated by the setup is approximately 45 mg of RuO_4 per hour.
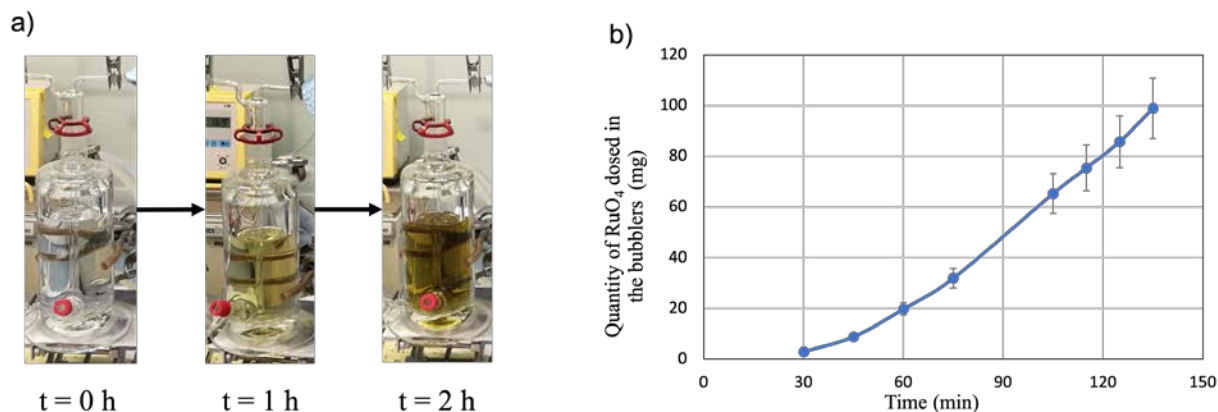
Figure 3. Monitoring the dissolution of $RuO_{4(g)}$ in a bubbler in an aqueous solution of NaOH (0.05 M) at 5°C.(a) Quantity of gaseous $RuO_{4(g)}$ generated by the setup during 135 min.(b)

Calculation of the decontamination factor (DF) of $RuO_{4(g)}$ by the MOF.

Decontamination factor (DF) of a filtration element (MOF) with respect to a pollutant ($RuO_{4(g)}$) is conventionally estimated by calculating the ratio of gaseous ruthenium concentrations in the gas flow upstream and downstream the MOF, according to equation 4.

$$DF\ (RuO_{4(g)}) = [RuO_{4(g)}]_{upstream}\ /\ [RuO_{4(g)}]_{downstream} \tag{4}$$

In this setup, these concentrations are not easily accessible simultaneously during a single test. Therefore, a multi-steps procedure was carried out to calculate accurately the DF.

The first step involves a blank test, under the desired experimental conditions and without the filtration element (i.e. without MOF) within the glass column. The second step corresponds to the "real" test, under strictly identical conditions to the blank test, but including the powdered MOF

within the glass column. Therefore, the decontamination factor of $RuO_{4(g)}$ is calculated using equation 5 (measurements downstream the glass column).

$$DF (RuO_{4(g)}) = [RuO_{4(g)}]_{blank} / [RuO_{4(g)}]_{real} \tag{5}$$

The total gas flow rate being the same during blank and "real" test, DF ($RuO_{4(g)}$) at a given time can also be calculated as the ratio of total amounts of RuO_4 cumulated at this time, for these two tests.

Theoretical calculations.

The evaluation of interaction energies between RuO_4 and the UiO-66 has been performed at the Density Functional Theory (DFT) level, using the Vienna Ab-initio Simulation Package (VASP).[31, 32] The electron-ion interactions are described using the Projector Augmented Wave (PAW) method of Blöchl[33], adapted by Kresse and Joubert.[34] The calculations were done at the Γ-point only due to the large size of the unit cells. The gradient corrected exchange correlation functional of Perdew, Burke and Ernzerhof (PBE) was employed.[35] The DFT-D3 correction method of Grimme and co-workers[36] was used in the present work, as implemented in VASP by Moellmann et Grimme,[37, 38] to estimate efficiently the dispersion forces. The wavefunction has been expanded in a plane wave basis set using a cutoff energy of 550 eV. The convergence parameters were set to 10^{-6} eV for the total energy and to 0.02 eV/Å for the residual forces on atoms. To improve electronic convergence, a Gaussian smearing with σ = 0.2 eV has been used. The frequencies have been determined numerically by diagonalization if the hessian matrix that is computed by a double displacement of the atoms in the three x, y, z, directions ($\Delta x = \pm 0.015$ Å). We have used our recently optimized cell[25] with the following parameters: $\alpha = \beta = \gamma = 90°$ and $a = b = c = 20.9$ Å to model the unit cell of UiO-66.

RESULTS.

UiO-66-NH$_2$ characterization.

The production of UiO-66-NH$_2$ has a yield of 60% based on the inorganic reactant ZrCl$_4$. The yellowish powder is well crystallized and does not contain traces of impurity based on PXRD analysis. ^{1}H NMR performed on the digested solid (Figure S1) allows to quantify the amount of BDC-NH$_2$ and formate ligands constituting the porous framework, and gives the followed formula for the dried solid Zr$_6$O$_4$(OH)$_4$(BDC-NH$_2$)$_{4,55}$(Form)$_{2.90}$ (BDC-NH$_2$ = 2-aminoterephtalate; Form = formate). The occurrence of formate ligands within the structure indicates that some aminoterephtalate linkers are substituted by formates. This difference compared to the ideal calculated structure Zr$_6$O$_4$(OH)$_4$(BDC-NH$_2$)$_6$ is a common feature in this family of MOFs and usually leads to a better pore accessibility compared to the no-defect structure.[39] The solid synthesized in this study exhibits a specific surface area (BET model) of 825 m^2.g^{-1} and a pore volume 0.31 m^3.g^{-1}. These values (>800 m^2/g) are in agreement with those usually reported in the literature.[40]

Filtration test and calculation of the decontamination factor.

When UiO-66NH$_2$ is placed in the filtration column under RuO$_{4(g)}$ flow, the breakthrough is observed between 75 and 105 min and characterized by the color change of the first bubbler, turning from colorless to yellow. The value of the DF is 569 ($\pm$ 97) after 30 min (Table 1), and the maximal value is measured before breakthrough after 75 min. At this time, DF is equal to 5745 ($\pm$ 977). Experiments realized on the same experimental setup and under the same conditions with sand, silver-doped zeolites and activated charcoal have shown a very low decontamination below 4.[7, 41] So, UiO-66-NH$_2$ is a much more promising material for the filtration of RuO$_4$.

Table 1. Decontamination factor (DF) for RuO_4 filtered by UiO-66-NH$_2$ at different contact times.

Time (min)	DF ($RuO_{4(g)}$)
30	569 ±97
45	1586 ± 270
60	3556 ± 605
75	5745 ± 977
105	1216 ± 207
115	216 ± 37
125	77 ± 13
135	35 ± 6

After 135 min, the generation of RuO_4 is stopped. At the end of the experiment, the saturation of the filter media after 135 min is also highlighted by the black coloration of UiO-66-NH$_2$, initially pale yellow (Figure 4a).

Characterization of the loaded-ruthenium MOF: Ru@UiO-66NH$_2$.

After the filtration study (135 min), the ruthenium impregnated MOF noted Ru@UiO-66-NH$_2$ was characterized by means of several techniques, to analyze the crystallinity of the composite material as well as the ruthenium chemistry within the pores.
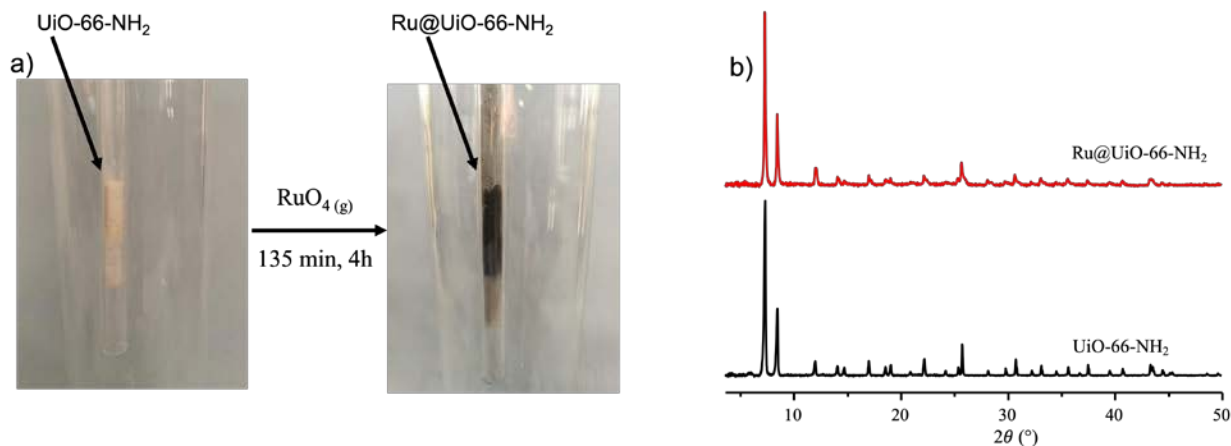
Figure 4. Photography of the filtering cell containing pristine UiO-66-NH$_2$ and after filtration of RuO$_4$ during 135 min at 50°C (a). Powder X-ray pattern of pristine and Ru-loaded UiO-66-NH$_2$ (b).

PXRD analysis (Figure 4b) measured at room temperature confirms the structural integrity of the UiO-66-NH$_2$ matrix and does not indicate the presence of additional crystallized phases in the sample like ruthenium oxides (RuOx). Furthermore, the typical octahedral-shaped of UiO-66-NH$_2$ crystal was not affected by RuO$_{4(g)}$ flow, confirming the excellent stability of the selected MOF under the experimental conditions. Whereas ruthenium oxide nanoparticles are used to precipitate easily at the surface of MOFs or other solids,[42] high resolution high angle annular dark field imaging does not show any traces of such particles or aggregates on the surface of the crystal. RuO$_2$ is the unique decomposition product from RuO$_4$, with a characteristic black color. Since it is the only ruthenium oxide stable and non-gaseous/volatile at room temperature, we argue that RuO$_2$ is the species trapped within the pore of UiO-66-NH$_2$. Furthermore, the conditions used in this study (relative low temperature and presence of water from RuO$_4$ precursor) and the precipitation of amorphous RuO$_2$, fit very well with the syntheses and the structural properties of ruthenium dioxide hydrates RuO$_2$.xH$_2$O.[43]

This claim will be confirmed later in the manuscript by transmission electron microscopy (no liberation of volatile species under vacuum) or NMR (large amount of water, presence of paramagnetic tetravalent ruthenium, instead of octavalent ruthenium in initial RuO_4 gas).

The homogeneous insertion of RuO_2 within the UiO-66-NH_2 crystallites is confirmed by Scanning Transmission Electron Microscopy-Energy Dispersive X-Xray spectroscopy mapping (STEM-EDS), since ruthenium and zirconium signals are overlapped (Figure 5). The deduced average composition gives an averaged molar ratio Ru/Zr close to 2 (estimated out of hundred UiO-66-NH_2 crystallites), in accordance with the following formula $Zr_6O_4(OH)_4(BDC\text{-}NH_2)_{4,55}(Form)_{2.90}\cdot(RuO_2)_{12}$.

Based on this formula, the trapping capacity of RuO_2 into UiO-66-NH_2 (Ru uptake) can be estimated at $0.985\ g_{(RuO2)}/g_{(UiO\text{-}66\text{-}NH2)}$ or $0.748\ g_{(Ru)}/g_{(UiO\text{-}66\text{-}NH2)}$. This value is slightly overestimated comparing to the estimation of Ru production during the test, based on ICP-AES measurements: $0.833\ g_{(RuO2)}/g_{(UiO\text{-}66\text{-}NH2)}$ or $0.633\ g_{(Ru)}/g_{(UiO\text{-}66\text{-}NH2)}$. This gap can be explained by a slightly higher RuO_2 concentration at the top of the UiO-66-NH_2 bed, where the TEM analyzed sample would come from.
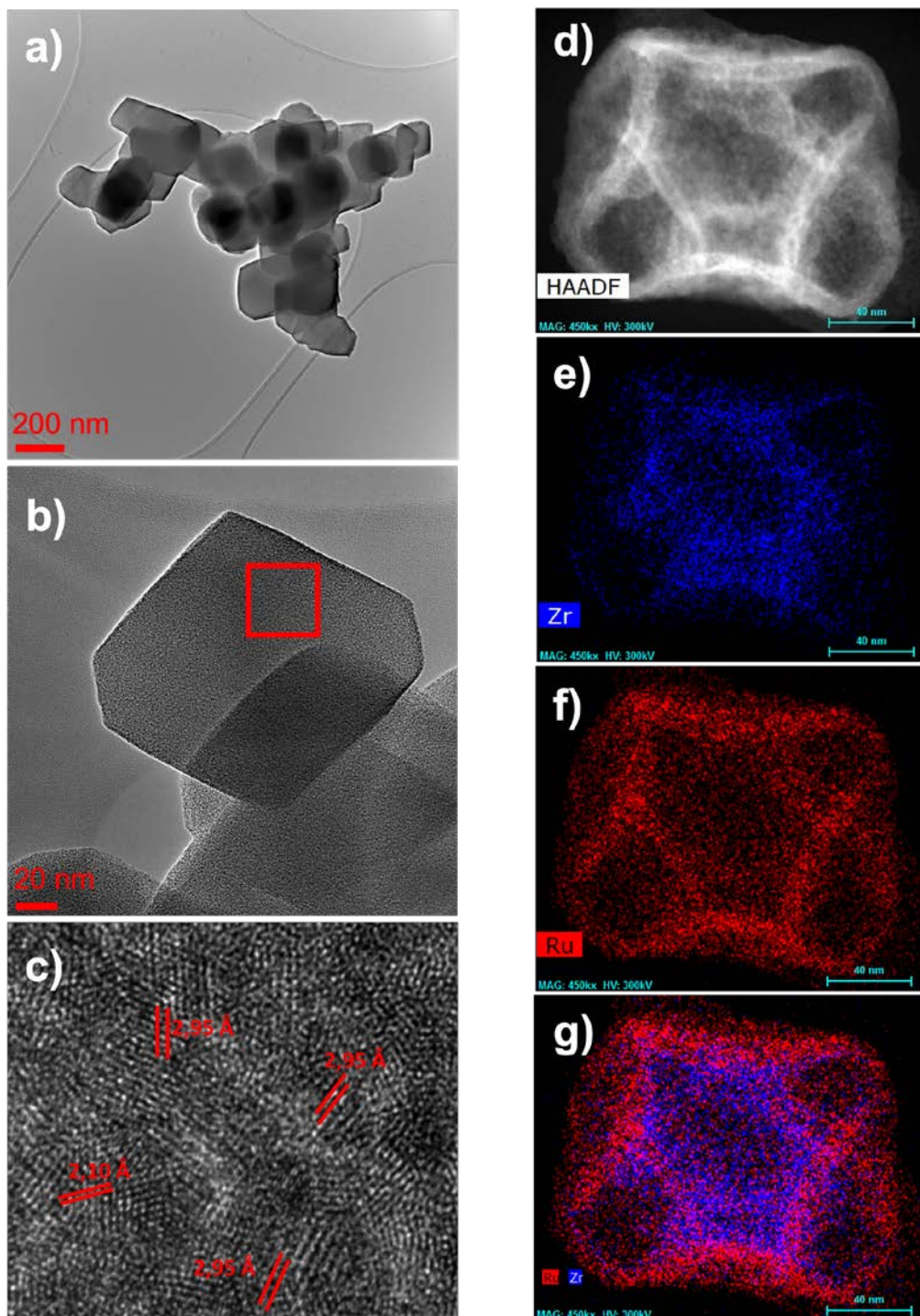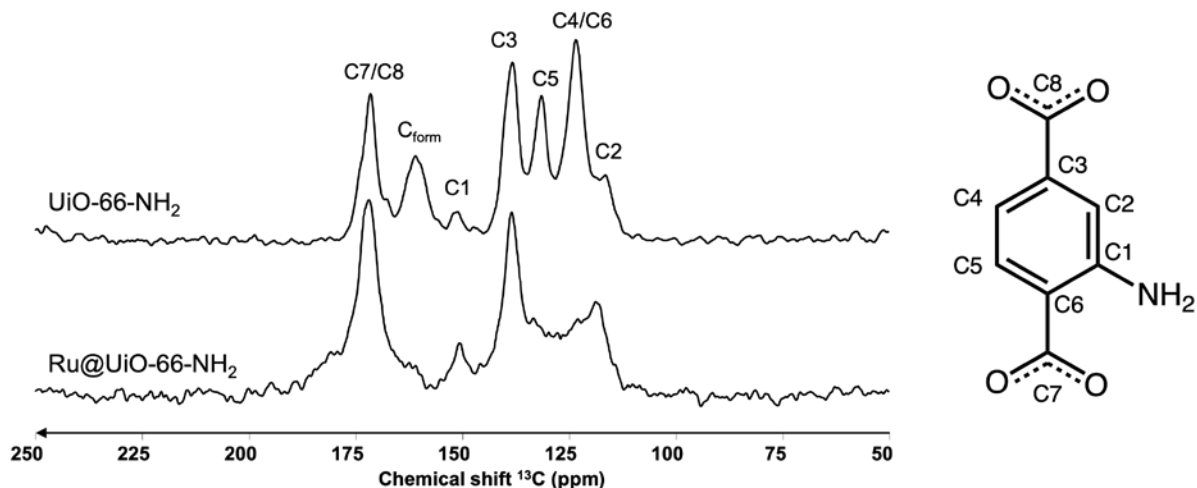
Figure 5. Ruthenium-loaded UiO-66-NH$_2$: a-c) TEM images (a, b). Enlargement showing crystallized nanodomains with interfringe spacing characteristic of ZrO$_2$. High-angle annular dark field (HAADF) image and corresponding EDS maps of Zr (e), Ru (f) and Ru+Zr (g).

TEM images of Ru-loaded UiO-66-NH$_2$ exhibit crystallized nanodomains characterized by fringes (2.1 and 2.95 Å), which are also observed in the as-made MOF and that do not fit with crystallized UiO-66-NH$_2$. Therefore, these domains cannot be attributed to RuO$_2$ which should occur within the framework as an amorphous ruthenium dioxide hydrate,[43] but correspond to interplanar spacing of ZrO$_2$ fluorite structure (d$_{111}$ = 2.956 Å and d112 = 2.09 Å).[44] The crystallization of zirconia is related to the local decomposition of the hybrid framework under the electron beam.

The structural integrity of Ru@UiO-66-NH$_2$ as well as the occurrence of paramagnetic Ru^{IV} from hydrated RuO$_2$ was confirmed by solid state NMR. Whereas ^{1}H spectrum is not exploitable due to a very large amount of trapped water molecules associated to RuO$_2$.xH$_2$O or trapped within the pores hiding the structural bands (Figure S2), ^{13}C analysis is not affected by this high hydration rate. The ^{13}C CPMAS NMR spectrum of the pristine UiO-66-NH$_2$ is characterized by six resonances associated to BDC-NH$_2$ linker and one to the formate ligand (Figure 6).[45]

The signal at 171 ppm is assigned to the two carboxylates functions C7 and C8 which are connected to the alpha carbons C6 and C3, resonating at 123 and 138 ppm, respectively. The C-H groups C2, C4 and C5 are characterized by the resonances at 117, 123 and 131 ppm, respectively. The last signal associated to the ligand corresponds to the carbon atom (C1) linked to the amino groups and resonates at 150 ppm. The presence of formate ligand (C$_{form}$) signal is emphasized by the signal at 160 ppm.

Figure 6. ^{13}C solid-state CPMAS NMR spectra of UiO-66-NH_2 (top) and ruthenium-loaded UiO-66-NH_2 (bottom). 9.4 T spectrometer, spinning rate at 12.5 kHz.

The ^{13}C CPMAS NMR spectrum is very disturbed after ruthenium inclusion since the signals associated to C4, C5, and C_{form} have disappeared from the initial spectrum, whereas those assigned to C1, C2, C3 are clearly not perturbated by the presence of ruthenium.

The fact that some signals associated to benzene rings are unchanged whereas others are removed confirms the stability of the structure, but indicates the proximity of a paramagnetic species (e.g. RuO_2) alongside specific carbon atoms (C4 and C5). This close interaction with paramagnetic RuO_2 is known to induce significant shift (several hundred ppm) for the nearest atoms.[46]

The same explanation can be used to explain the disappearance of the peak associated to formate ligand (C_{form}). However, the departure of this single carbon-based molecule and its oxidation into CO_2 cannot be ruled out, based on NMR results. This mechanism is analogous to that of the decomposition of formic acid activated by ruthenium-catalysts (RuO_2 or $RuCl_3$).[47-49]

Thermal behavior of ruthenium-loaded UiO-66-NH₂

To confirm the presence of stable RuO_2 within the framework, instead of a volatile species such as RuO_4, we analyzed the thermal resistance of Ru@UiO-66-NH₂ solid.
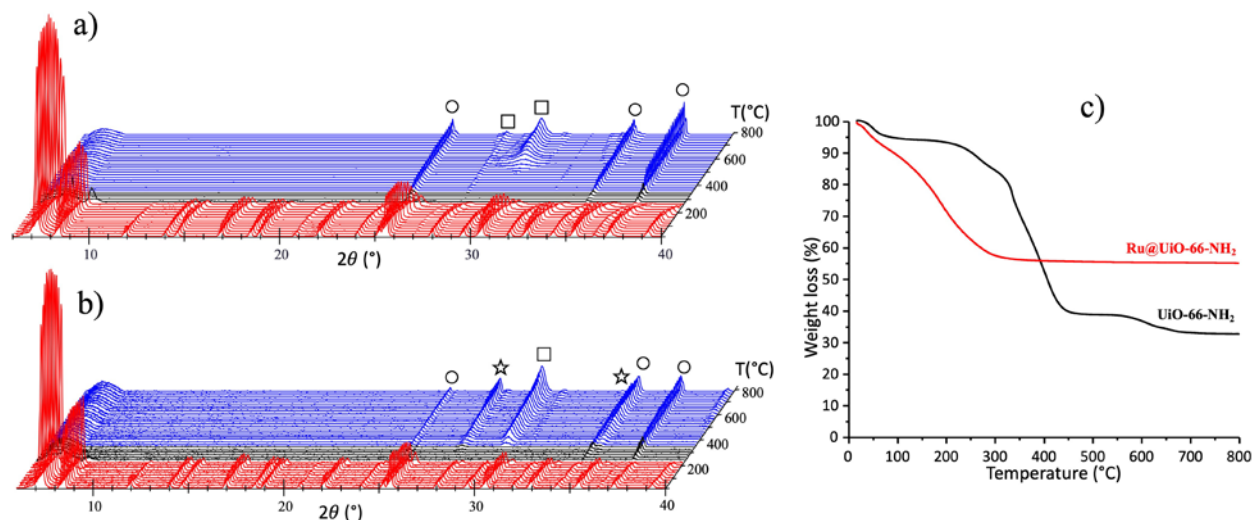
Figure 7. Evolution of the powder X-ray diffraction patterns under air of pristine UiO-66-NH₂ (a) and ruthenium-loaded UiO-66-NH₂ (b) as a function of temperature. Circle, square and star represent diffraction peaks of Al_2O_3 sample holder, ZrO_2 and RuO_2, respectively. Thermogravimetric curves (c) of UiO-66-NH₂ and ruthenium-loaded UiO-66-NH₂ under air atmosphere (5°C/min).

Whereas pristine UiO-66-NH₂ is stable up to 260°C under air (Figure 7a), the introduction of ruthenium oxide within the solid decreases the thermal stability down to 220°C (Figure 7b). In this last case, the thermal degradation leads to the crystallization of ZrO_2 (pdf file : 04-013-3441) and RuO_2 (PDF file 04-009-8496), separately. The different behavior is even more obvious by thermal gravimetric analysis (TGA) (Figure 7c). Pure UiO-66-NH₂ shows three distinctive weight losses, successively assigned to the departure of trapped solvent (from RT to 100°C), the thermal decomposition of the organic ligand (from 250°C to 400°C) and the dehydroxylation process (from 500°C to 600°C), respectively. Only one step is observed for the Ru@UiO-66-NH₂ sample,

occurring from RT to 250°C. This single event is ascribed to the departure of organic ligand as well as water molecules (from solvent trapped into the pores, MOF dihydroxylation and/or hydrated RuO_2) and leads to a final plateau corresponding to a mixture of crystallized ZrO_2 and RuO_2 (Figure S3). Owing to an unclear weight loss distinction between the different constituents of the Ru@UiO-66-NH$_2$, no attempt for calculation has been made.

The quicker decomposition of the loaded UiO-66-NH$_2$ is associated to the presence of RuO_2 which acts as an oxidative catalyst for the decomposition of the hybrid compound. This behavior is very similar to that of organic compounds transformation into gases (CO_2, CH_4, H_2), catalyzed by RuO_2 at high temperature in supercritical water.[50]

RuO$_4$ behavior after trapping within UiO-66-NH$_2$

The different methods of characterization used for this study indicate that ruthenium is trapped as stable form within UiO-66-NH$_2$. Since RuO_4 is a highly volatile species, which could decompose into nonvolatile RuO_2,[51] we suppose that this last oxide is predominant inside the UiO-66-NH$_2$ pores. Whereas other stable ruthenium oxides could exist (RuO, RuO_3), these species are only stable as gaseous form at very high temperature (>1000°C),[52] incompatible with the classic MOF stability.[2]

As indicated by NMR spectroscopy, the introduction of RuO_4 within the pores leads to the disappearance of ^{13}C NMR signals (C4 and C5) of aminoterephtalate ligands. This change is associated to the presence of paramagnetic Ru(IV) oxide close to the accessible carbons atoms around the benzene ring.

The proximity between aminoterephtalate ligand and RuO_4 is easily explained by a classical 3+2 Diels-Alder reaction (5) (Figure 8). This type of reaction has been studied for OsO_4[53, 54] or RuO_4[55] on simple aromatic systems or double bonds. DFT calculation confirms the good affinity between the ditopic ligand of UiO-66-NH$_2$ and RuO_4, through strong hydrogen bonding between the porous framework (from NH_2 groups connected to neighboring ligands) and the gaseous species in intermediate 1.

The 3+2 Diels-Alder reaction (2) is endothermic ($\Delta rE=0,63$ eV) as the hydrogen bond between the RuO_4 and the amines are broken during the process. This transformation leads to the reduction of Ru(VIII) into Ru(IV) and is related to the oxidation of benzene ring into a catecholate group, connected to RuO_2 in intermediate 3. In the following step, protons are displaced from the tetrahedral carbon to restore the aromaticity of the benzene ring (intermediate 4). The displacement of the two protons is exothermic ($\Delta rE=-1.46$ eV and ($\Delta rE=-1.43$ eV for the first and second displacement, respectively). The oxidation of the aromatic ring is strongly exothermic ($\Delta rE=-2,26$ eV). The most suitable position of the proton is on the carboxylic group, since the catechol configuration is less stable (0.42 eV). The RuO_2 formed during the reaction, is coordinated to the two OH groups which enhances their acidity and favors the displacement of the protons on the carboxylic acid. This mechanism is in perfect agreement with the solid-state NMR characterization, assuming the proximity of C4 and C5 with ruthenium atom.

To confirm the formation of the protonated carboxylate function, we computed the vibrational frequencies of the linker before and after oxidation. In our model, the wave numbers of C=O stretching mode are increased by 160 cm^{-1} compared to the non-protoned linker. The addition of proton on the carbonyl group increases the C-OH distance by 0.07 Å (1,34 vs. 1,27 Å) and a

reduction of the second C=O bond by 0.04 Å (1,23 Å vs. 1,27 Å), which explains the evolution of the wave numbers.

As expected, a blue shift is observed on the experimental infrared spectrum of Ru@UiO-66-NH_2 by a new band visible at 1868 cm^{-1}, involving a shift of 288 cm^{-1} (Figure S4). The difference between the experimental and the calculated values is assigned to the presence of RuO_2 aggregates within the pores (and not isolated RuO_2 species as calculated), that could modify structural vibrations.
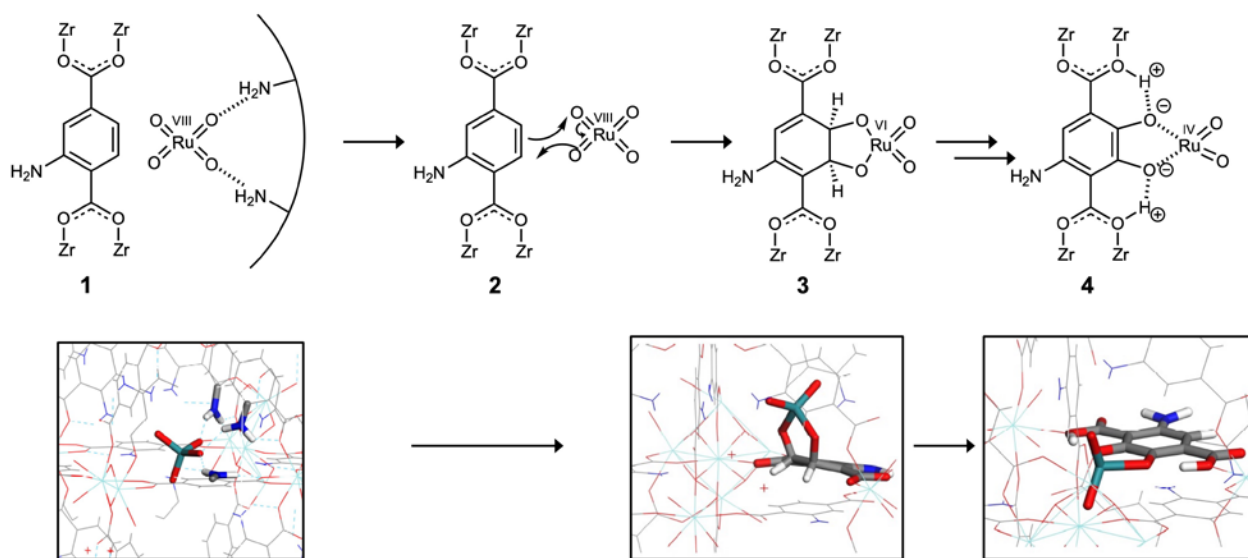
Figure 8. Mechanisms of reactivity of RuO_4 with aminoterephtalate ligands highlighted by structural configurations extracted from DFT calculations.

CONCLUSION.

For the first time, a Metal-Organic Framework (UiO-66-NH_2) compound was used for the capture of gaseous ruthenium tetroxide RuO_4, which may exhibit radiotoxic isotopes in case of power plant

nuclear accident. Since gaseous RuO_4 is not commercially available, we developed a specific installation to produce this gas as well as the quantification of RuO_4 trapped within the filtering medium. UiO-66-NH_2 has a remarkable affinity for RuO_4 capture, since this MOF exhibits the worldwide highest RuO_4 decontamination factor (DF up to 5745), hundreds of times higher than the DF values of sorbents daily used by the nuclear industry (zeolites or activated charcoal).

The efficiency of UiO-66-NH_2 is explained by its pores diameter well adapted to the capture and the immobilization of RuO_4, as well as its conversion into stable hydrated ruthenium dioxide ($RuO_2.xH_2O$) within the pores. This conversion corresponds to the reactivity of RuO_4 with the MOF organic sub-network, leading to the decomposition of formate ligands as well as the oxidation of terephthalate ligands. As proved by powder X-ray diffraction or NMR, these modifications do not decompose the MOF structure. However, the presence of catalytic RuO_2 within the pores slightly accelerates the thermal decomposition of this solid, when increasing temperature from 220°C (instead of 260°C for the pristine UiO-66-NH_2 phase). As a future work, additional techniques like X-ray Photoelectron Spectrometry (XPS) or X-ray absorption spectroscopies (EXAFS/XANES) would be used to analyze the oxidation state of ruthenium within the MOF.

Whereas UiO-66-NH_2 exhibits the best decontamination factor for RuO_4, the efficiency of this MOF needs to be confirmed under more relevant accidental conditions, involving high temperature, steam or radiation. Moreover, the resistance of UiO-66-NH_2 versus beta emitter like 103/106-Ru needs to be confirmed. A very recent publication about the excellent resistance of Al-based MOF303[56] is very promising for the capture of such isotopes.

ASSOCIATED CONTENT

Supporting Information.

Additional PXRD, infrared and ^{1}H NMR analysis.

AUTHOR INFORMATION

Corresponding Author

Christophe VOLKRINGER – Univ. Lille, CNRS, Centrale Lille, UMR 8181 – UCCS-U ité de Catalyse et Chimie du Solide, Lille F-59000, France

Email : christophe.volkringer@centralelille.fr

Author Contributions

The manuscript was written through contributions of all authors. All authors have given approval to the final version of the manuscript.

REFERENCES

1.   I. Zuba, M. Zuba, M. Piotrowski and A. Pawlukojc, *Appl. Radiat. Isot.*, 2020, **162**.
2.   C. Mun, L. Cantrel and C. Madic, *Nucl. Technol.*, 2006, **156**, 332-346.

3.   O. Masson, G. Steinhauser, D. Zok, O. Saunier, H. Angelov, D. Babic, V. Beckova, J. Bieringer, M. Bruggeman, C. I. Burbidge, S. Conil, A. Dalheimer, L. E. Geer, A. D. Ott, K. Eleftheriadis, S. Estier, H. Fischer, M. G. Garavaglia, C. G. Leonarte, K. Gorzkiewicz, D. Hainz, I. Hoffman, M. Hyza, K. Isajenko, T. Karhunen, J. Kastlander, C. Katzlberger, R. Kierepko, G. J. Knetsch, J. K. Konyi, M. Lecomte, J. W. Mietelski, P. Min, B. Moller, S. P. Nielsen, J. Nikolic, L. Nikolovska, I. Penev, B. Petrinec, P. P. Povinec, R. Querfeld, O. Raimondi, D. Ransby, W. Ringer, O. Romanenko, R. Rusconi, P. R. J. Saey, V. Samsonov, B. Silobritiene, E. Simion, C. Soderstrom, M. Sostaric, T. Steinkopff, P. Steinmann, I. Sykora, L. Tabachnyi, D. Todorovic, E. Tomankiewicz, J. Tschiersch, R. Tsibranski, M. Tzortzis, K. Ungar, A. Vidic, A. Weller, H. Wershofen, P. Zagyvai, T. Zalewska, D. Z. Garcia and B. Zorko, *Proc. Nati. Acad. Sci. USA*, 2019, **116**, 16750-16759.

4.   M. W. Cooke, A. Botti, D. Zok, G. Steinhauser and K. R. Ungar, *Proc. Nati. Acad. Sci. USA*, 2020, **117**, 14703-14711.

5.   B. J. Riley, J. D. Vienna, D. M. Strachan, J. S. McCloy and J. L. Jerden, Jr., *J. Nuc. Mater.*, 2016, **470**, 307-326.

6.   P. Swain, C. Mallika, R. Srinivasan, U. K. Mudali and R. Natarajan, *J. Radioanal. Nucl. Chem.*, 2013, **298**, 781-796.

7.   P. Nerisson, H. Hu, J. F. Paul, L. Cantrel and C. Vesin, *J. Radioanal. Nucl. Chem.*, 2019, **321**, 591-598.

8.   D. Jacquemain, *NEA/CSNI/R(2014)7*, 2014.

9.   F. Kepak, S. Koutova, M. Kocirik and A. Zikanova, *J. Radioanal. Nucl. Chem.*, 1992, **159**, 317-334.

10.   F. Kepak, S. Koutova and J. Kanka, *Isotopenpraxis*, 1990, **26**, 73-78.

11.   F. Kepak, J. Kanka and S. Koutova, *Isotopenpraxis*, 1985, **21**, 58-62.

12.   J. R. Long and O. M. Yaghi, *Chem. Soc. Rev.*, 2009, **38**, 1213-1214.

13.   H. Furukawa, K. E. Cordova, M. O'Keeffe and O. M. Yaghi, *Science*, 2013, **341**, 974-+.

14.   G. M. Tom, W. Morris, M. H. Weston, P. E. Fuller, P. W. Siu, C. R. Murdock, J. P. Siegfried and O. K. Farha, *2016 21st International Conference on Ion Implantation Technology (Iit)*, 2016.

15.   C. L. Xiao, M. A. Silver and S. Wang, *Dalton Trans.*, 2017, **46**, 16381-16386.

16.   C. Falaise, C. Volkringer, R. Giovine, B. Prelot, M. Huve and T. Loiseau, *Dalton Trans.*, 2017, **46**, 12010--12014.

17.   C. Lai, Z. H. Wang, L. Qin, Y. K. Fu, B. S. Li, M. M. Zhang, S. Y. Liu, L. Li, H. Yi, X. G. Liu, X. R. Zhou, N. An, Z. W. An, X. X. Shi and C. L. Feng, *Coord. Chem. Rev.*, 2021, **427**.

18.   M. Leloire, J. Dhainaut, P. Devaux, O. Leroy, H. Desjonqueres, S. Poirier, P. Nerisson, L. Cantrel, S. Royer, T. Loiseau and C. Volkringer, *J. Hazardous Mater.*, 2021, **416**.

19.   N. N. Shen, Z. X. Yang, S. T. Liu, X. Dai, C. L. Xiao, K. Taylor-Pashow, D. E. Li, C. Yang, J. Li, Y. G. Zhang, M. X. Zhang, R. H. Zhou, Z. F. Chai and S. Wang, *Nat. Commun.*, 2020, **11**.

20.   D. P. Sheng, L. Zhu, X. Dai, C. Xu, P. Li, C. I. Pearce, C. L. Xiao, J. Chen, R. H. Zhou, T. Duan, O. K. Farha, Z. F. Chai and S. Wang, *Angew. Chem. Int. Ed.*, 2019, **58**, 4968-4972.

21. L. Zhu, D. P. Sheng, C. Xu, X. Dai, M. A. Silver, J. Li, P. Li, Y. X. Wang, Y. L. Wang, L. H. Chen, C. L. Xiao, J. Chen, R. H. Zhou, C. Zhang, O. K. Farha, Z. F. Chai, T. E. Albrecht-Schmitt and S. Wang, *J. Am. Chem. Soc.*, 2017, **139**, 14873-14876.

22. C. Volkringer, C. Falaise, P. Devaux, R. Giovine, V. Stevenson, F. Pourpoint, O. Lafon, M. Osmond, C. Jeanjacques, B. Marcillaud, J. C. Sabroux and T. Loiseau, *Chemical Communications*, 2016, **52**, 12502-12505.

23. R. Giovine, F. Pourpoint, S. Duval, O. Lafon, J. P. Arnoureux, T. Loiseau and C. Volkringer, *Cryst. Growth Des.*, 2018, **18**, 6681-6693.

24. M. Leloire, C. Walshe, P. Devaux, R. Giovine, S. Duval, T. Bousquet, S. Chibani, J. F. Paul, A. Moissette, H. Vezin, P. Nerisson, L. Cantrel, C. Volkringer and T. Loiseau, *Chem. Eur. J.*

25. S. Chibani, M. Badawi, T. Loiseau, C. Volkringer, L. Cantrel and J. F. Paul, *PhysChemChemPhys*, 2018, **20**, 16770-16776.

26. S. J. Garibay and S. M. Cohen, *Chem. Commun.*, 2010, **46**, 7700-7702.

27. D. F. Sava, M. A. Rodriguez, K. W. Chapman, P. J. Chupas, J. A. Greathouse, P. S. Crozier and T. M. Nenoff, *J. Am. Chem. Soc.*, 2011, **133**, 12398-12401.

28. K. W. Chapman, D. F. Sava, G. J. Halder, P. J. Chupas and T. M. Nenoff, *J. Am. Chem. Soc.*, 2011, **133**, 18583-18585.

29. B. M. Fung, A. K. Khitrin and K. Ermolaev, *J. Magn. Reson.*, 2000, **142**, 97-101.

30. R. P. Larsen and L. E. Ross, *Anal. Chem.*, 1959, **31**, 176-178.

31. G. Kresse and J. Hafner, *Phys. Rev. B*, 1993, **47**, 558-561.

32. J. Hafner, *J. Comput. Chem.*, 2008, **29**, 2044-2078.

33. P. E. Blochl, *Phys. Rev. B*, 1994, **50**, 17953-17979.

34. G. Kresse and D. Joubert, *Phys. Rev.B*, 1999, **59**, 1758-1775.

35. J. P. Perdew, K. Burke and M. Ernzerhof, *Phys. Rev. Lett.*, 1996, **77**, 3865-3868.

36. S. Grimme, J. Antony, S. Ehrlich and H. Krieg, *J. Chem. Phys.*, 2010, **132**.

37. J. Moellmann and S. Grimme, *Phys. Chem. Chem. Phys.*, 2010, **12**, 8500-8504.

38. S. Grimme, *Wiley Interdiscip. Rev. Comput. Mol. Sci.*, 2011, **1**, 211-228.

39. G. C. Shearer, S. Chavan, S. Bordiga, S. Svelle, U. Olsbye and K. P. Lillerud, *Chem. Mater.*, 2016, **28**, 3749-3761.

40. G. Hoyez, J. Rousseau, C. Rousseau, S. Saitzek, J. King, P. A. Szilagyi, C. Volkringer, T. Loiseau, F. Hapiot, E. Monflier and A. Ponchel, *CrystEngComm*, 2021, **23**, 2764-2772.

41. P. Nerisson, M. Barrachin, L. Cantrel and M. Philippe, Seattle (WA), 2019.

42. T. S. Wang, L. J. Gao, J. W. Hou, S. J. A. Herou, J. T. Griffiths, W. W. Li, J. H. Dong, S. Gao, M. M. Titirici, R. V. Kumar, A. K. Cheetham, X. H. Bao, Q. Fu and S. K. Smoukov, *Nature Commun.*, 2019, **10**.

43. D. A. McKeown, P. L. Hagans, L. P. L. Carette, A. E. Russell, K. E. Swider and D. R. Rolison, *J. Phys. Chem. B*, 1999, **103**, 4825-4832.

44. S. Khalili and H. M. Chenari, *J. Alloys Compd.*, 2020, **828**.

45. S. Devautour-Vinot, G. Maurin, C. Serre, P. Horcajada, D. P. da Cunha, V. Guillerm, E. D. Costa, F. Taulelle and C. Martineau, *Chem. Mater.*, 2012, **24**, 2168-2177.

46. K. Kitagawa, K. Ishida, R. S. Perry, H. Murakawa, K. Yoshimura and Y. Maeno, *Phys. Rev. B*, 2007, **75**.

47. M. Czaun, A. Goeppert, J. Kothandaraman, R. B. May, R. Haiges, G. K. S. Prakash and G. A. Olah, *Acs Catal.*, 2014, **4**, 311-320.

48. T. Sheng, J. Y. Ye, W. F. Lin and S. G. Sun, *Phys. Chem. Chem. Phys.*, 2017, **19**, 7476-7480.
49. W. Chen, L. P. Xu and S. W. Chen, *J. Electroanal. Chem.*, 2009, **631**, 36-42.
50. K. C. Park and H. Tomiyasu, *Chem. Commun.*, 2003, 694-695.
51. C. Mun, L. Cantrel and C. Madic, *Radiochim. Acta*, 2007, **95**, 643-656.
52. F. Miradji, S. Souvi, L. Cantrel, F. Louis and V. Vallet, *J. Phys. Chem. A*, 2015, **119**, 4961-4971.
53. A. Poethig and T. Strassner, *J. Org. Chem.*, 2010, **75**, 1967-1973.
54. A. A. Hussein, M. J. S. Phipps, C. K. Skylaris and R. C. D. Brown, *J. Org. Chem.*, 2019, **84**, 15173-15183.
55. E. Nowicka, N. W. Hickey, M. Sankar, R. L. Jenkins, D. W. Knight, D. J. Willock, G. J. Hutchings, M. Francisco and S. H. Taylor, *Chem. Eur. J.*, 2018, **24**, 12359-12369.
56. X. Z. Chen, X. J. Liu, S. T. Xiao, W. J. Xue, X. D. Zhao and Q. Y. Yang, *Sep. Purif. Technol.*, 2022, **297**.

SYNOPSIS (Word Style "SN_Synopsis_TOC"). If you are submitting your paper to a journal

that requires a synopsis, see the journal's Instructions for Authors for details.